

pubs.acs.org/JPCL Letter

Investigating Tunneling-Controlled Chemical Reactions through Ab Initio Ring Polymer Molecular Dynamics

Xinyang Li and Pengfei Huo*



Cite This: J. Phys. Chem. Lett. 2021, 12, 6714-6721



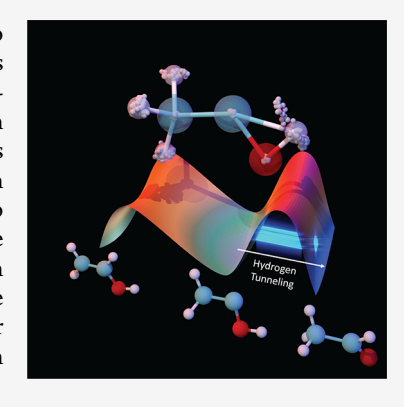
ACCESS

III Metrics & More



SI Supporting Information

ABSTRACT: We use the ab initio ring polymer molecular dynamics (RPMD) approach to investigate tunneling-controlled reactions in methylhydroxycarbene. Nuclear tunneling effects enable molecules to overcome the barriers which cannot be overcome classically. Under low-temperature conditions, intrinsic quantum tunneling effects can facilitate the chemical reaction in a pathway that is favored neither thermodynamically nor kinetically. This behavior is referred to as the tunneling-controlled chemical reaction and is regarded as the third paradigm of chemical reaction controls. In this work, we use the ab initio RPMD approach to incorporate the tunneling effects in our quantum dynamics simulations and investigate the reaction kinetics of two competitive reaction pathways at various temperatures. The reaction rate constants obtained here agree extremely well with the experimentally measured rates. We demonstrate the feasibility of using ab initio RPMD rate calculations in a realistic molecular system and provide an interesting and important example for future investigations of reaction mechanisms dominated by quantum tunneling effects.



uclear quantum effects (NQEs), such as quantum tunneling and gore retunneling and zero-point energy (ZPE), have been shown to play a crucial role in various chemical processes, 1,2 including hydrogen bonding,^{3–7} proton transfer reactions,^{8–10} hydride transfer reactions,^{11,12} proton-coupled electron transfer (PCET) reactions,^{13–16} and catalytic reactions.^{17–20} NQEs enable molecules to directly tunnel through the potential energy barriers that are otherwise formidably high classically.²¹ Although the importance of tunneling effects in chemistry has long been acknowledged,²² the attention on the ability to actively use tunneling to control chemical reaction directions has only begun to emerge recently. 23-26 Tunneling control refers to the scenarios where a kinetically or thermodynamically less favored reaction pathway becomes the dominating one due to reaction enhancement by intrinsic quantum tunneling effects. 23-26 This phenomenon has been recently regarded as the third paradigm of chemical reaction control, beyond the traditional thermodynamic and kinetic controls.²

Methylhydroxycarbene (MHC), a hydroxycarbene derivative, has emerged as an excellent example of tunneling-controlled reactions. There are two hydrogen atom transfer pathways to the divalent carbon atom in MHC, as illustrated in Figure 1. We denote reaction pathway A as the hydrogen atom transfer from the methyl group to the carbine center, forming vinyl alcohol; and reaction pathway B as the transfer of the hydrogen atom in the hydroxy group to the carbine center, resulting in acetaldehyde. Both reactions cause the decay of the MHC molecule. At low temperatures, the decay of MHC results in acetaldehyde through reaction B, forming a product that is favored neither kinetically nor thermodynamically. This leads to a completely tunneling-

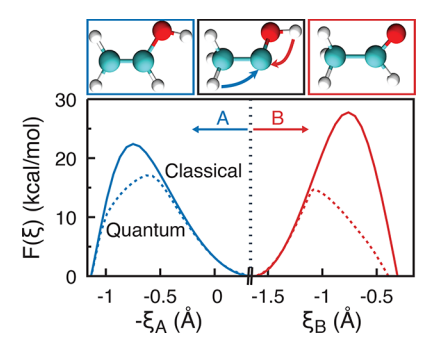


Figure 1. Classical (solid lines) and quantum (dashed lines) free energy profiles $F(\xi)$ as a function of the reaction coordinate ξ at 200 K for both reaction pathways A (blue) and B (red). The geometries in the top panel correspond to vinyl alcohol (product A), methylhydroxycarbene (reactant), and acetaldehyde (product B), respectively. The arrows show the transferring direction of the hydrogen atoms. Note that to indicate the HAT direction of reaction A, $-\xi_A$ is used as the x-axis in this plot.

controlled product.^{23–26} Many more recent examples of tunneling-controlled reactions can be found in a recent review in ref 26. Accurately simulating the tunneling-controlled

Received: May 22, 2021 Accepted: July 6, 2021



chemical reaction requires an explicit description of the NQEs, which is beyond classical rate constant theory or classical molecular dynamics simulation.

In this work, we use ring polymer molecular dynamics $(RPMD)^{10,28-31}$ to compute the reaction rate constants for two competing reaction paths in the MHC molecule. RPMD is an approximate quantum dynamics approach based on Feynman's imaginary-time path-integral formalism, 32 which provides exact quantum statistics and approximate yet accurate quantum dynamics. 28,33,34 In this formalism, each atom is represented by a ring polymer of n beads (imaginary-time slices), with a harmonic spring connecting the adjacent beads. 35

Quantum reaction rate constants can be accurately evaluated using the RPMD flux-side correlation function formalism, which has been extensively discussed in the previous literature. Here, we demonstrate perhaps the first ab initio RPMD rate constant calculation. We combine RPMD with ab initio on-the-fly simulations at the level of Kohn—Sham DFT (with the BLYP functional APPRO and in its singlet state) using a plane-wave basis to investigate the competing hydrogen atom transfer (HAT) reactions in MHC. The computational details are provided in the section Theoretical and Computational Approaches.

For a molecular system with N total nuclear degrees of freedom (DOF) (or $\frac{1}{3}N$ total number of atoms), the corresponding ring polymer Hamiltonian is expressed as

$$H_n(\mathbf{p}, \mathbf{q}) = \sum_{j=1}^n \left[\frac{\mathbf{p}_j^2}{2\mathbf{M}} + V(\mathbf{q}_j) + \frac{1}{2} \mathbf{M} \omega_n^2 (\mathbf{q}_j - \mathbf{q}_{j-1})^2 \right]$$
(1)

where n is the total number of copies (beads) of the original s y s t e m , a n d $\mathbf{q}_j = \{[q_1]_j, [q_2]_j, ..., [q_N]_j\}$ a n d $\mathbf{p}_j = \{[p_1]_j, [p_2]_j, ..., [p_N]_j\}$ are the position and momentum vectors of the j_{th} bead, respectively, with mass $\mathbf{M} = \{M_1, M_2, ..., M_N\}$. Further, $V(\mathbf{q}_j)$ is the adiabatic potential energy surface for the nuclei, and the interbead ring polymer frequency is $\omega_n = n/\beta\hbar$.

The approximate quantum mechanical rate constant is calculated as the plateau value of the RPMD flux-side correlation function. ^{10,28,31} To facilitate numerical simulations, we apply the Bennett–Chandler scheme that expresses the rate constant as follows ^{10,13,36}

$$k = \lim_{t \to t_{p}} \kappa(t) \cdot k_{\text{QTST}}$$
 (2)

where $t_{\rm p}$ refers to the plateau time of the flux-side correlation function, $k_{\rm QTST}$ is the RPMD-Transition State Theory (TST) rate constant which has been shown to be equivalent to the quantum TST (QTST) rate constant, and $\kappa(t)$ is the transmission coefficient that captures the dynamical recrossing effect. The details of $k_{\rm TST}$ are provided in the section Theoretical and Computational Approaches at the end of this Letter, and $\kappa(t)$ is expressed as follows

$$\kappa(t) = \frac{\langle \mathcal{F} \cdot h[\xi(\overline{\mathbf{q}}_t) - \xi^{\ddagger}] \rangle_c}{\langle \mathcal{F} \cdot h[\dot{\xi}(\overline{\mathbf{q}}_0)] \rangle_c}$$
(3)

where $\overline{\mathbf{p}} = \frac{1}{n} \sum_{j} \mathbf{p}_{j}$ and $\overline{\mathbf{q}} = \frac{1}{n} \sum_{j} \mathbf{q}_{j}$ are the centroids of the momenta and positions, respectively. The 0 and t subscripts in

 ${\bf q}$ indicate the initial time and time t. In addition, h is the side operator, which is a Heaviside function of the reaction coordinate ξ that differentiates the reactant versus the product, and ${\mathcal F}$ is the flux operator which is the time derivative of the side operator ${\mathcal F}({\bf q}_0, {\bf p}_0) = \dot h[\xi({\bf q}_0)]$. Further, $\langle \cdots \rangle_c$ denotes the ensemble average over trajectories that are initially constrained on the dividing surface ξ^{\ddagger} . The dividing surface is chosen as the collective coordinate that maximizes the potential of mean force. ^{10,40} Note that the RPMD rate is proven to be dividing surface independent. ^{30,31}

The transmission coefficients as well as the free energy profiles are evaluated with the ring polymer trajectories governed by the RPMD Hamiltonian \hat{H}_n in eq 1, whereas the potential $V(\mathbf{q}_i)$ is evaluated through ab initio on-the-fly simulations. The largest $\kappa(t)$ simulation of this work requires the on-the-fly propagation of a $\frac{1}{3}N \times n = 7*64 = 448$ -atom fictitious molecular ring-polymer for up to 10³ trajectories, with at least 450 electronic structure calculations along every single ring polymer trajectory. Additional details of the numerical simulations are provided in the section Theoretical and Computational Approaches. Using the ab initio RPMD approach combined with the enhanced sampling technique (the blue moon ensemble approach, 42-44 see details in the Supporting Information), we can directly compute the classical (when using n = 1) and quantum mechanical free energy profiles (potential of mean force).

The RPMD rate is closely connected with the instanton rate constant, which has been extensively discussed by Althorpe and co-workers. 45,46 The instanton rate constant can be derived on the basis of a steepest descent approximation of the quantum flux-side correlation function, 46-48 resulting in $k_{\rm inst} = A_{\rm inst} e^{-S/\hbar}$, where $A_{\rm inst}$ is a prefactor and $S = \int_0^{\beta h} d\tau \left[\frac{M}{2} |\dot{q}|^2 + V(q) \right]$ is the Euclidean action (in the imaginary time τ and $\dot{q}=dq/d\tau)$ measured along the instanton trajectory $q(\tau)$. The ring-polymer potential $\sum\nolimits_{j=1}^{N} \left[V(\mathbf{q}_j) + \frac{1}{2} \mathbf{M} \omega_n^2 (\mathbf{q}_j - \mathbf{q}_{j-1})^2 \right] \text{ in } H_n \text{ (eq 1) is simply a}$ discretized version of S/\hbar . For a symmetric system, the ring polymer beads at the dividing surface describe a finitedifference approximation to the "instanton" trajectory, which is a periodic orbit in imaginary time on the inverted potential surface. 45,46 The instanton theory also qualitatively explains the tunneling-controlled reactivities: If two mechanisms are competing, the one that minimizes the value of S will dominate the product, not necessarily the one with a lower potential barrier as predicted by classical TST.46 Only under the classical limit (high temperature or low barrier frequency) does k_{inst} reduce to the classical TST rate and the potential barrier dictate the rate.46

We note that molecular reactions of the MHC molecule have been investigated with the instanton theory in ref 27. The instanton theory employed in that work is based on a steepest descent approximation (harmonic approximations for the thermal fluctuations) for all nuclear DOFs. The steepest-descent approximation used in the instanton theory is not valid for systems with large anharmonicity. This potential issue of steepest descent can be partially addressed by using the so-called free energy instanton theory, specifically where the steepest descent approximation is only applied to the reaction coordinate. However, this approach requires computing the

quantum free energy profile, with the computational cost equivalent to the RPMD-TST rate constant calculation. As extensively investigated in ref 50., the RPMD-TST rate is generally more accurate than the free energy instanton calculation over all temperatures, especially for multidimensional molecular systems. In this paper, explicit dynamical recrossing is also considered by computing the transmission coefficient. For these reasons, RPMD is the most widely applicable of these path-integral rate methods.

Figure 1 presents the classical potential of mean force (solid

curves) and the quantum potential of mean force (dashed curve) $F(\xi)$ (defined in eq 5) at T = 200 K, along the reaction coordinate ξ (defined in eq 4) for both reaction A (blue) and B (red). It is clear that the classical free energy barrier of pathway B is higher than reaction A but also thinner than pathway A. Compared with the classical free energy barrier, the quantum free energy barriers are significantly lower for both reaction pathways. Further, reaction B is now having an even lower free energy barrier than reaction A. This is because the NOEs start to dominate the reaction mechanism below the crossover temperatures 45 $T_{\rm C}=\frac{\hbar\omega^{\ddagger}}{2\pi k_{\rm B}}$ where ω^{\ddagger} is the imaginary barrier frequency at the transition state (TS), and tunneling is more sensitive to the barrier width, rather than the potential barrier height. The crossover temperatures were reported to be 321 and 462 K for pathways A and B, respectively.²⁷ Since tunneling effects are essential to the reaction mechanism below the crossover temperature, this highlights the importance of using a method which includes tunneling effects in the

Figure 2A provides the typical configurations of the molecular ring polymer along the reaction coordinate of reaction B. The labels for each configuration indicate a particular value of $\xi_{\rm B}$ in panel B. At the transition state ensemble, the ring polymer spans over the barrier into the reactant and product sides. The reaction pathway B allows most of the beads to reach lower potential positions, due to a thinner potential barrier. Since the ring polymer radius is particularly large when T is small (due to the lower ω_n in H_n of eq 1), this effect plays an essential role at low temperatures in lowering the effective potential that the ring polymer feels, resulting in a lower free energy barrier.

simulations of this system.

Figure 2B presents free energy profiles $F(\xi)$ at 200 K of reaction pathway B, computed with the classical ab initio MD (AIMD) with n = 1 (red) and the quantum RPMD with n = 32 (blue). Apparently, without considering NQEs, classical AIMD overestimates the free energy barrier height by more than 10 kcal/mol.

After reaching the TS configuration (II in Figure 2A), the molecular ring polymer goes into a "sliding downhill" process, as it appears that it directly cuts through the barrier. This is because at such a low temperature, the ring polymer is overstretched (III in Figure 2A), and the top of the free energy barrier, based on the centroid coordinate, is no longer able to represent an optimized dividing surface that minimizes recrossing. This causes the maximum of the free energy to deviate from the maximum of the potential energy surface for an asymmetric double-well system. We emphasize that this is a well-known feature of RPMD, which does not significantly influence the accuracy of the rate constant so long as $\kappa(t)$ (which accounts for the recrossing) is also explicitly included in the rate constant.

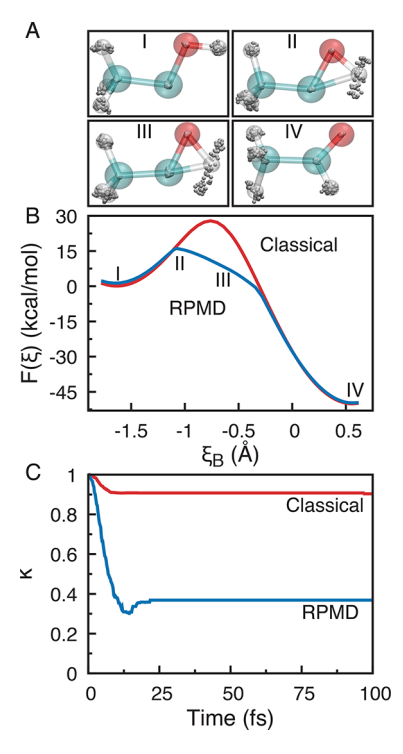


Figure 2. Simulation results for reaction pathway B at 200 K. (A) The typical ring polymer configurations of the reactant (I), TS (II), product (IV), as well as a configuration (III) between the TS and product. (B) The classical (red) and quantum (blue) free energy profiles $F(\xi)$ as a function of the reaction coordinate B ξ_B . (C) The classical (red) and quantum (blue) transmission coefficients $\kappa(t)$.

Figure 2C presents the classical and quantum time-dependent transmission coefficients $\kappa(t)$ at 200 K for the reaction pathway B. At short times, there is a "tug of war" on the centroid between the vibrating ring polymer beads in the reactant and product wells, which results in a pronounced oscillation in the transmission coefficient. The plateau value $\kappa(t_{\rm p})$ is lower in the quantum simulation compared with the classical one. 11,13

To investigate the temperature dependence of the rate constant, we also perform the simulations at T=400, 300, and 120 K for reaction pathway B. Similarly, we computed these quantities for reaction pathway A. These additional results are provided in the Supporting Information (Figure S1). Figure 3A presents the ring polymer transition state configurations at four temperatures. The radius of the ring polymer for all atoms increases as the temperature decreases, because the spring constant of the ring polymer becomes weaker ($\omega_n \propto T$). As a result, the ring polymer of the transferring hydrogen atom becomes more stretched on the top of the potential barrier, indicating a stronger tunneling effect.

Figure 3B presents the temperature dependence of the free energy profile along the reaction coordinate $\xi_{\rm B}$. As we expected, the free energy barrier becomes lower at a lower temperature. As we have discussed previously, when the temperature is below $\frac{1}{2}T_{\rm c}$ (half of the crossover temperature), there is a clear "edge cutting" behavior along the reaction coordinate, which originates from evaluating the free energy profile with a centroid coordinate.

Figure 3C presents the transmission coefficients $\kappa(t)$ computed under four different temperatures. Not surprisingly, the plateau value $\kappa(t_{\rm p})$ decreases at as temperature drops

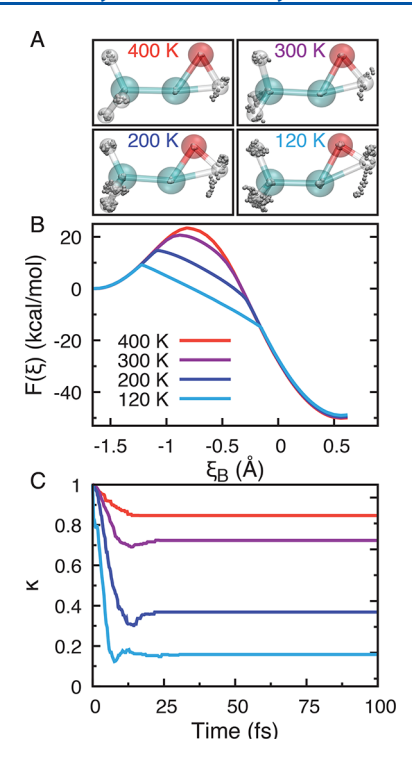


Figure 3. Temperature-dependence of reaction pathway B. (A) The representative ring polymer TS configurations at four different temperatures. (B) The quantum free energy profiles $F(\xi)$ as a function of the reaction coordinate B ξ_B at four temperatures corresponding to panel A. The free energy barrier $\Delta F(\xi^{\ddagger})$ decreases as the temperature decreases. (C) The time-dependent transmission coefficient $\kappa(t)$ plots at four different temperatures. The plateau value $\kappa(t_{\rm p})$ decreases as the temperature decreases.

because of lowered barriers and the complex motion of the overstretched ring polymer in the intermediate time, which leads to more recrossing events. The relatively low value of $\kappa(t_{\rm p})$ at 200 K and below also clearly indicates that the top of the free energy barrier based on the centroid coordinate is no longer an optimized dividing surface that minimize recrossing. 45,50

Figure 4 presents the plots of the rate constant for the reaction pathway A (blue) and B (red), obtained by plugging

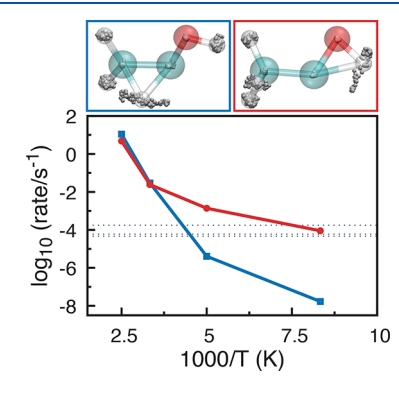


Figure 4. Temperature dependence of the rate constants k for pathway A (blue) and pathway B (red). Note that the base-10 logarithm is used for plotting log k. Three horizontal black dotted lines present experimentally measured rates at 11 K in three different hosting matrices.²³ The top panels show the typical ring polymer configurations of pathways A and B, respectively.

 $k_{\rm TST}$ computed from the free energy barrier heights and the plateau value of the transmission coefficients $\kappa(t_{\rm p})$ into eq 2. There exists a crossover of the two rate constants in the temperature range between 200 and 300 K, indicating a switch in the preferred reaction mechanism. Under the high-temperature limit, the free energy barrier of reaction pathway A is much lower than the barrier of pathway B (by around 5 kcal/mol at T=400 K). Consequently, the reaction rate of pathway A is higher in this case, making vinyl alcohol the preferred product.

Under lower-temperature conditions, the quantum free energy barriers for both pathways decrease. However, as shown in Figure 1, the barrier of the pathway B drops much faster than that of pathway A. As a result, tunneling effects reduce the effective free energy barrier of pathway B more significantly. Given the fact that $\kappa(t_{\rm p})$ of both pathways are at the same magnitude at the same temperature (see Figure 3C and Figure S1B in the Supporting Information), the preferred pathway will be reverted to pathway B at low temperatures.

Figure 4 also clearly demonstrates that for T < 200 K, nuclear quantum effects start to dominate the reaction rate. Recall that the classical TST theory (Eyring equation) gives $\ln\frac{k}{T} = -\frac{\Delta H^{\ddagger}}{k_{\rm B}} \cdot \frac{1}{T} + \frac{\Delta S^{\ddagger}}{k_{\rm B}} + \ln\frac{k_{\rm B}}{h}$, where $h = 2\pi\hbar$ is the Planck constant, and ΔH^{\ddagger} and ΔS^{\ddagger} are the activation enthalpy and entropy (per molecule), respectively. Hence, $-\frac{\Delta H^{\ddagger}}{k_{\rm B}}$ gives the effective slope of the Eyring plot and $\frac{\Delta S^{\ddagger}}{k_{\rm B}} + \ln\frac{k_{\rm B}}{h}$ is the intercept on the y axis. Thus, if the reaction is dominated by the classical thermal activation process, log k will be a linear function of 1/T, with the slope of $-\frac{\Delta H^{\ddagger}}{k_{\rm B}}$. Apparently, this is not the case for the rate constant presented in this figure, as the log k starts to plateau with a larger 1/T, which is a common indicator of the tunneling dominate regime. $\frac{2.5,52,53}{k_{\rm B}}$

Our theoretical results of the rate constant at a very low temperature T = 120 K agree with the experimental observations that acetaldehyde is the preferred product, which is measured under T = 11 K within three different hosting matrices (Ar, Kr, and Xe), with corresponding rate constants (black dashed lines) presented in Figure 4. Although we are comparing our 120 K results with the experimental data at 11 K, T = 120 K is already far below $\frac{1}{2}T_c$, half of the crossover temperatures of both pathways. This means that the thermally induced contribution to the reaction rate is minimal and further decreasing the temperature will not change the reaction rate, hence log k should plateau as a function of 1/Tas we have discussed previously. This is why our numerical results have already shown the trend of approaching the plateau value in Figure 4. Interestingly, the ratio of the two rate constants in the plateau region of deep tunneling from our calculation is log $k_B/k_A = 3.7$, in a good agreement with the experimentally 23 measured value 3.3 under T = 11 K.

Simulating lower temperature results (T < 120 K) requires even more beads (n > 64) in the ring polymer and, consequently, more computational resources. In the future, this can be addressed by incorporating the ring polymer contraction scheme, ^{54,55} where the full ring polymer beads potential is evaluated with some lower level electronic structure calculations (such as the Density Functional based Tight Binding) as a "reference" system, while a contracted ring polymer is evaluated with the higher level theory (such as KS-

DFT), hence saving a huge amount of computational efforts, as demonstrated in the recent state-of-the-art AIMD-RPMD simulation of water. S4,55 Another potential challenge arises from the fact that the centroid coordinate deviates from the optimal dividing surface for low temperatures, resulting in a numerically small plateau value of $\kappa(t_{\rm p})$ (that might even be close to 0), which requires a large number of trajectories to converge. This can be potentially addressed by incorporating the knowledge from other noncentroid modes into the collective coordinate. 30,31,45

In conclusion, we have reported, to the best of our knowledge, the first ab initio on-the-fly RPMD rate constant calculation. We use it to investigate tunneling-controlled reactions in methylhydroxycarbene. We computed the free energy profiles and reaction rate constants of two hydrogen transfer pathways in methylhydroxycarbene. Our results suggest that below the crossover temperature, intrinsic quantum tunneling effects can facilitate the chemical reaction in a pathway that is neither favored thermodynamically nor kinetically, opening up new possibilities to enable chemical transformations. Further, our ab initio RPMD rate constant calculations provide accurate rate constants of the reactions that are in excellent agreement with the experimental measurements.²³ We demonstrated that RPMD can be conveniently combined with ab initio on-the-fly simulations to investigate a realistic hydrogen atom transfer system under the tunneling-controlled reaction regime. This work provides an interesting and important example of using ab initio RPMD to investigate reactions dominated by quantum tunneling effects²⁶ to provide detailed mechanistic insights.

THEORETICAL AND COMPUTATIONAL APPROACHES

All simulations, including the free energy profile and transmission coefficient calculations, are performed with an in-house modified version of the CPMD⁵⁶ package version 3.15.3. The molecule is simulated with the BLYP functional^{37–39} in its singlet electronic ground state. The molecule is placed in an isolated simulation box of 8 Å which is treated with Martyna—Tuckerman formalism,⁵⁷ and a plane-wave basis with a cutoff of 80 Ry. The core electrons were treated with Troullier—Martins pseudopotentials.⁵⁸ The normal mode representation of the ring polymer is used to propagate the trajectories in all simulations.⁵⁹

To characterize the progress of the reaction, we use the following reaction coordinate

$$\xi(\mathbf{q}) = \frac{\mathbf{R}_{\mathrm{DH}} \cdot \mathbf{R}_{\mathrm{DA}}}{|\mathbf{R}_{\mathrm{DA}}|} = \frac{(\mathbf{q}_{\mathrm{H}} - \mathbf{q}_{\mathrm{D}}) \cdot (\mathbf{q}_{\mathrm{A}} - \mathbf{q}_{\mathrm{D}})}{|\mathbf{q}_{\mathrm{A}} - \mathbf{q}_{\mathrm{D}}|} \tag{4}$$

where H, D, and A denote the transferring hydrogen atom, the donor atom, and the acceptor atom, respectively. This reaction coordinate measures the length of the projection of vector \mathbf{R}_{DH} onto the axis that connects the hydrogen donor and acceptor atoms. The larger the reaction coordinate is, the closer the transferring hydrogen is to the acceptor atom. For the RPMD simulations, the centroid coordinate $\overline{\mathbf{q}} = \frac{1}{n} \sum_j \mathbf{q}_j$ is used in the above expression.

The potential of mean force (PMF) $F(\xi)$ at reaction coordinate ξ^i is defined as

$$F(\xi^{i}) = -\frac{1}{\beta} \ln \left[\frac{C_{\mathcal{N}}}{Q(N, V, T)} \int d\mathbf{p} d\mathbf{q} e^{-\beta H_{n}(\mathbf{p}, \mathbf{q})} \delta(\xi - \xi^{i}) \right]$$
(5)

where $H_n(\mathbf{p}, \mathbf{q})$ is the ring polymer Hamiltonian defined in eq 1, $C_N = \frac{1}{(N/3)! h^N}$, and $Q(N, V, T) = \int d\mathbf{p} d\mathbf{q} e^{-\beta H_n(\mathbf{p}, \mathbf{q})}$ is the ring polymer canonical partition function. The PMF is computed using path-integral Car-Parrinello molecular dynamics (CPMD) simulations. The fictitious electron mass m = 400 au is used in the CPMD-PIMD simulations. A massive Nosé-Hoover chain thermostat⁶⁰ on every nuclear DOF is used to maintain a NVT ensemble in the simulation box. The path-integral molecular dynamics (PIMD)⁶¹ propagation is used for the nuclei, using fictitious nuclear masses (Parrinello-Rahman mass) that are 4 times their respective physical masses to facilitate the sampling of the ring polymer configurations. We have carefully checked that the CPMD generated PMF is identical to the Born-Oppenheimer MD generated PMF for both the classical dynamics and the PIMD dynamics, with results provided in the Supporting Information. Since the free energy barriers for both pathways are much higher compared to thermal fluctuations, ²³ the blue moon ensemble approach ^{42–44} (an enhanced sampling technique) is used to facilitate the free energy calculations in the canonical (NVT) ensemble. The details of the blue moon ensemble simulation are provided in the Supporting Information. A set of 40 constrained MD simulations are performed along the reaction coordinate from the reactant to the product in the NVT ensemble. The time step is set to be 0.072 fs. Each trajectory is then equilibrated for at least 0.5 ps, followed by a production run of at least 1 ps.

A rough estimation of the number of beads needed can be obtained using $n > \hbar \omega_{\rm max}/k_{\rm B}T$, where $\omega_{\rm max}$ is the maximum frequency of the molecule. Normal mode analysis at the level of B3LYP/cc-pVTZ using Gaussian 09 package gives $\omega_{\rm max} = 3826~{\rm cm}^{-1}$ (the O–H bond stretching frequency) for the MHC molecule. This leads to n = 28 for $T = 200~{\rm K}$ and n = 46 for $T = 120~{\rm K}$. The number of beads n used for nuclei quantization in the actual simulations at various temperatures are listed in Table 1. We have carefully checked the bead convergence, with details provided in the Supporting Information.

Table 1. Number of Beads Used at Different Temperatures in Our Simulations

T (K)	400	300	200	120
n	16	16	64	64

The ring polymer molecular dynamics transition state theory (RPMD-TST) rate constant $k_{\rm TST}$ accounts for the rate component purely dictated by quantum statistics (quantum free energy barrier height). It has been shown that $k_{\rm TST}$ coincide with the quantum mechanical TST rate theory, explaining the success of the RPMD rate theory. The RPMD-TST rate $k_{\rm TST}$ is expressed as

$$k_{\text{TST}} = \frac{1}{2\pi\beta} \langle g_{\xi} \rangle_{c} \frac{e^{-\beta\Delta F(\xi^{\dagger})}}{\int_{-\infty}^{\xi^{\dagger}} e^{-\beta\Delta F(\xi)} d\xi}$$
(6)

where $\xi(\overline{\mathbf{q}})$ denotes the centroid reaction coordinate (defined in eq 4), ξ^{\ddagger} denotes the value of the dividing surface along the

reaction coordinate, which is obtained at the highest value of $F(\xi(\overline{\mathbf{q}}))$ along $\xi(\overline{\mathbf{q}})$, and $\Delta F(\xi^{\ddagger})$ represents the free energy barrier height from the bottom of the reactant well to the top of the free energy barrier at $\xi = \xi^{\ddagger}$. Further,

$$g_{\xi}(\overline{\mathbf{q}}) = \sqrt{\sum_{i=1}^{N} \frac{1}{M_i} \left(\frac{\partial \xi(\overline{\mathbf{q}})}{\partial \overline{q}_i}\right)^2}$$
, where i is the index of the nuclear

DOF, M_i is the corresponding mass, and N is the total number of DOF. This quantity serves as the square root of the inverse reduced mass of the reaction coordinate.

To compute $\kappa(t)$ in eq 3, one needs to define the following side operator h, which is a Heaviside function of the reaction coordinate ξ defined as

$$h[\xi(\overline{\mathbf{q}}_{t})] = \begin{cases} 1, & \text{if } \xi \geqslant \xi^{\ddagger} \\ 0, & \text{if } \xi < \xi^{\ddagger}. \end{cases}$$

$$(7)$$

The flux operator is the time derivative of the side operator, expressed as

$$\mathcal{F}(\overline{\mathbf{q}}_{0'}, \overline{\mathbf{p}}_{0}) = \dot{h}[\xi(\overline{\mathbf{q}}_{0})] = \sum_{i=1}^{N} \delta(\xi - \xi^{\ddagger}) \frac{d\xi}{d\overline{q}_{i}} \overline{p}_{i}$$
(8)

A constrained canonical ensemble on the dividing surface $\xi = \xi^{\ddagger}$ is generated to calculate the transmission coefficient κ . In our simulations, these configurations are generated by propagating a sampling trajectory constrained on the ring polymer centroid dividing surface $\xi(\overline{\bf q}) = \xi^{\ddagger}(\overline{\bf q})$, through the SHAKE algorithm implemented in the CPMD package. The constrained geometries are picked at every 0.36 ps from the sampling trajectory.

The transmission coefficient κ is calculated using the aforementioned configurations as the initial configurations and by releasing them from the dividing surface at $\xi(\overline{\mathbf{q}})$. The initial velocities are sampled from the Maxwell-Boltzmann distribution. The dynamics is propagated in the NVE ensemble (without any thermostat), using RPMD in the normal mode representation with the physical masses of the nuclei. Due to the fact that the highest normal-mode frequency $\omega_n = n/\beta\hbar$ in RPMD will be close to the fictitious electronic frequencies in CPMD, the adiabaticity condition in CPMD method is no longer valid. As a result, all the trajectories for computing $\kappa(t)$ are simulated with Born-Oppenheimer molecular dynamics (BOMD) as implemented in the CPMD package. Between 500 and 1200 trajectories are released from the dividing surfaces, where each RPMD trajectory is evolved for 100 fs (during which the flux-side correlation function is guaranteed to reach the plateau value) with a time step of 0.24 fs.

ASSOCIATED CONTENT

Supporting Information

The Supporting Information is available free of charge at https://pubs.acs.org/doi/10.1021/acs.jpclett.1c01630.

Computational details, additional results for reaction pathway A, choice of the density functional, tests of bead convergence, free energy profiles computed from different approaches (PDF)

AUTHOR INFORMATION

Corresponding Author

Pengfei Huo – Department of Chemistry, University of Rochester, Rochester, New York 14627, United States; orcid.org/0000-0002-8639-9299; Email: pengfei.huo@rochester.edu

Author

Xinyang Li – Department of Chemistry, University of Rochester, Rochester, New York 14627, United States

Complete contact information is available at: https://pubs.acs.org/10.1021/acs.jpclett.1c01630

Notes

The authors declare no competing financial interest.

ACKNOWLEDGMENTS

This work was supported by the National Science Foundation CAREER Award under Grant No. CHE-1845747. Computing resources were provided by the Center for Integrated Research Computing (CIRC) at the University of Rochester, as well as by XSEDE under Grant No. CHE-190016. The authors appreciate valuable comments to the manuscript from Eric Koessler.

REFERENCES

- (1) Markland, T. E.; Ceriotti, M. Nuclear Quantum Effects Enter the Mainstream. *Nat. Rev. Chem.* **2018**, *2*, 0109.
- (2) Hammes-Schiffer, S. Quantum Effects in Complex Systems: Summarizing Remarks. *Faraday Discuss.* **2020**, 221, 582–588.
- (3) Kawashima, Y.; Tachikawa, M. Nuclear quantum effect on intramolecular hydrogen bond of hydrogen maleate anion: An ab initio path integral molecular dynamics study. *Chem. Phys. Lett.* **2013**, *571*, 23–27.
- (4) Fang, W.; Chen, J.; Rossi, M.; Feng, Y.; Li, X.-Z.; Michaelides, A. Inverse Temperature Dependence of Nuclear Quantum Effects in DNA Base Pairs. *J. Phys. Chem. Lett.* **2016**, *7*, 2125–2131.
- (5) Litman, Y.; Richardson, J. O.; Kumagai, T.; Rossi, M. Elucidating the Nuclear Quantum Dynamics of Intramolecular Double Hydrogen Transfer in Porphycene. *J. Am. Chem. Soc.* **2019**, *141*, 2526–2534.
- (6) Pérez, A.; Tuckerman, M. E.; Hjalmarson, H. P.; von Lilienfeld, O. A. Enol Tautomers of Watson-Crick Base Pair Models Are Metastable Because of Nuclear Quantum Effects. *J. Am. Chem. Soc.* **2010**, *132*, 11510–11515.
- (7) Ceriotti, M.; Fang, W.; Kusalik, P. G.; McKenzie, R. H.; Michaelides, A.; Morales, M. A.; Markland, T. E. Nuclear Quantum Effects in Water and Aqueous Systems: Experiment, Theory, and Current Challenges. *Chem. Rev.* **2016**, *116*, 7529–7550.
- (8) Hammes-Schiffer, S.; Tully, J. C. Proton transfer in solution: Molecular dynamics with quantum transitions. *J. Chem. Phys.* **1994**, *101*, 4657–4667.
- (9) Roberts, S. T.; Ramasesha, K.; Petersen, P. B.; Mandal, A.; Tokmakoff, A. Proton Transfer in Concentrated Aqueous Hydroxide Visualized Using Ultrafast Infrared Spectroscopy. *J. Phys. Chem. A* **2011**, *115*, 3957–3972.
- (10) Collepardo-Guevara, R.; Craig, I. R.; Manolopoulos, D. E. Proton Transfer in a Polar Solvent from Ring Polymer Reaction Rate Theory. *J. Chem. Phys.* **2008**, *128*, 144502–144514.
- (11) Boekelheide, N.; Salomón-Ferrer, R.; Miller, T. F., III Dynamics and Dissipation in Enzyme Catalysis. *Proc. Natl. Acad. Sci. U. S. A.* **2011**, *108*, 16159–16163.
- (12) Suleimanov, Y. V.; Collepardo-Guevara, R.; Manolopoulos, D. E. Bimolecular reaction rates from ring polymer molecular dynamics: application to H + CH $_4$ \rightarrow H $_2$ + CH $_3$. *J. Chem. Phys.* **2011**, *134*, 044131–044140.
- (13) Kretchmer, J. S.; Miller, T. F. Direct Simulation of Proton-coupled Electron Transfer across Multiple Regimes. *J. Chem. Phys.* **2013**, *138*, 134109–134128.
- (14) Hammes-Schiffer, S.; Soudackov, A. V. Proton-coupled Electron Transfer in Solution, Proteins, and Electrochemistry. *J. Phys. Chem. B* **2008**, *112*, 14108–14123.

- (15) Hazra, A.; Soudackov, A. V.; Hammes-Schiffer, S. Role of Solvent Dynamics in Ultrafast Photoinduced Proton-coupled Electron Transfer Reactions in Solution. *J. Phys. Chem. B* **2010**, *114*, 12319—12332.
- (16) Hazra, A.; Soudackov, A. V.; Hammes-Schiffer, S. Isotope Effects on the Nonequilibrium Dynamics of Ultrafast Photoinduced Proton-Coupled Electron Transfer Reactions in Solution. *J. Phys. Chem. Lett.* **2011**, *2*, 36–40.
- (17) Benkovic, S. J.; Hammes-Schiffer, S. A Perspective on Enzyme Catalysis. *Science* **2003**, *301*, 1196–1202.
- (18) Zhang, C.; Michaelides, A. Quantum Nuclear Effects on the Location of Hydrogen above and below the Palladium (100) Surface. *Surf. Sci.* **2011**, *605*, *689*–*694*.
- (19) Cendagorta, J. R.; Powers, A.; Hele, T. J. H.; Marsalek, O.; Bačić, Z.; Tuckerman, M. E. Competing Quantum Effects in the Free Energy Profiles and Diffusion Rates of Hydrogen and Deuterium Molecules through Clathrate Hydrates. *Phys. Chem. Chem. Phys.* **2016**, 18, 32169–32177.
- (20) McIntosh, E. M.; Wikfeldt, K. T.; Ellis, J.; Michaelides, A.; Allison, W. Quantum Effects in the Diffusion of Hydrogen on Ru(0001). *J. Phys. Chem. Lett.* **2013**, *4*, 1565–1569.
- (21) Hund, F. Zur Deutung der Molekelspektren. Iii. Eur. Phys. J. A 1927, 43, 805–826.
- (22) Wigner, E. On the Quantum Correction for Thermodynamic Equilibrium. *Phys. Rev.* **1932**, *40*, 749–759.
- (23) Schreiner, P. R.; Reisenauer, H. P.; Ley, D.; Gerbig, D.; Wu, C.-H.; Allen, W. D. Methylhydroxycarbene: Tunneling Control of a Chemical Reaction. *Science* **2011**, *332*, 1300–1303.
- (24) Ley, D.; Gerbig, D.; Wagner, J. P.; Reisenauer, H. P.; Schreiner, P. R. Cyclopropylhydroxycarbene. *J. Am. Chem. Soc.* **2011**, *133*, 13614–13621.
- (25) Ley, D.; Gerbig, D.; Schreiner, P. R. Tunnelling Control of Chemical Reactions the Organic Chemist's Perspective. *Org. Biomol. Chem.* **2012**, *10*, 3781—3790.
- (26) Schreiner, P. R. Tunneling Control of Chemical Reactions: The Third Reactivity Paradigm. *J. Am. Chem. Soc.* **2017**, *139*, 15276–15283.
- (27) Kästner, J. Path Length Determines the Tunneling Decay of Substituted Carbenes. *Chem. Eur. J.* **2013**, *19*, 8207–8212.
- (28) Habershon, S.; Manolopoulos, D. E.; Markland, T. E.; Miller, T. F. Ring-Polymer Molecular Dynamics: Quantum Effects in Chemical Dynamics from Classical Trajectories in an Extended Phase Space. *Annu. Rev. Phys. Chem.* **2013**, *64*, 387–413.
- (29) Craig, I. R.; Manolopoulos, D. E. Quantum Statistics and Classical Mechanics: Real Time Correlation Functions from Ring Polymer Molecular Dynamics. *J. Chem. Phys.* **2004**, *121*, 3368–3373.
- (30) Craig, I. R.; Manolopoulos, D. E. Chemical Reaction Rates from Ring Polymer Molecular Dynamics. *J. Chem. Phys.* **2005**, *122*, 084106–084117.
- (31) Craig, I. R.; Manolopoulos, D. E. A Refined Ring Polymer Molecular Dynamics Theory of Chemical Reaction Rates. *J. Chem. Phys.* **2005**, *123*, 034102–034111.
- (32) Feynman, R.; Hibbs, A. R. Quantum Mechanics and Path Integrals; McGraw-Hill: New York, NY, 1965.
- (33) Hele, T. J. H.; Willatt, M. J.; Muolo, A.; Althorpe, S. C. Boltzmann-conserving Classical Dynamics in Quantum Time-correlation Functions: "matsubara Dynamics. *J. Chem. Phys.* **2015**, 142, 134103–134115.
- (34) Hele, T. J. H.; Willatt, M. J.; Muolo, A.; Althorpe, S. C. Communication: Relation of Centroid Molecular Dynamics and Ringpolymer Molecular Dynamics to Exact Quantum Dynamics. *J. Chem. Phys.* **2015**, *142*, 191101–191105.
- (35) Chandler, D.; Wolynes, P. G. Exploiting the Isomorphism between Quantum Theory and Classical Statistical Mechanics of Polyatomic Fluids. *J. Chem. Phys.* **1981**, 74, 4078–4095.
- (36) Menzeleev, A. R.; Ananth, N.; Miller, T. F. Direct Simulation of Electron Transfer Using Ring Polymer Molecular Dynamics: Comparison with Semiclassical Instanton Theory and Exact Quantum Methods. *J. Chem. Phys.* **2011**, *135*, 074106–074122.

- (37) Becke, A. D. Density-functional Exchange-energy Approximation with Correct Asymptotic Behavior. *Phys. Rev. A: At., Mol., Opt. Phys.* **1988**, 38, 3098–3100.
- (38) Colle, R.; Salvetti, O. Approximate Calculation of the Correlation Energy for the Closed Shells. *Theor. Chim. Acta* **1975**, 37, 329–334.
- (39) Lee, C.; Yang, W.; Parr, R. G. Development of the Colle-Salvetti Correlation-energy Formula into a Functional of the Electron Density. *Phys. Rev. B: Condens. Matter Mater. Phys.* **1988**, 37, 785–789
- (40) Frenkel, D.; Smit, B. Understanding Molecular Simulation; Elsevier: San Diego, CA, 2002.
- (41) Hele, T. J. H.; Althorpe, S. C. Derivation of a true ($t \to 0^+$) quantum transition-state theory. I. Uniqueness and Equivalence to Ring-polymer Molecular Dynamics Transition-state-theory. *J. Chem. Phys.* **2013**, *138*, 084108–084120.
- (42) Carter, E. A.; Ciccotti, G.; Hynes, J. T.; Kapral, R. Constrained Reaction Coordinate Dynamics for the Simulation of Rare Events. *Chem. Phys. Lett.* **1989**, *156*, 472–477.
- (43) Sprik, M.; Ciccotti, G. Free Energy from Constrained Molecular Dynamics. J. Chem. Phys. 1998, 109, 7737–7744.
- (44) Laria, D.; Ciccotti, G.; Ferrario, M.; Kapral, R. Activation Free Energy for Proton Transfer in Solution. *Chem. Phys.* **1994**, *180*, 181–180
- (45) Richardson, J. O.; Althorpe, S. C. Ring-polymer Molecular Dynamics Rate-theory in the Deep-tunneling Regime: Connection with Semiclassical Instanton Theory. *J. Chem. Phys.* **2009**, *131*, 214106–214117.
- (46) Richardson, J. O. Perspective: Ring-polymer Instanton Theory. *J. Chem. Phys.* **2018**, *148*, 200901–200908.
- (47) Richardson, J. O. Ring-polymer Instanton Theory. *Int. Rev. Phys. Chem.* **2018**, 37, 171–216.
- (48) Makarov, D. E.; Topaler, M. Quantum Transition-state Theory below the Crossover Temperature. *Phys. Rev. E: Stat. Phys., Plasmas, Fluids, Relat. Interdiscip. Top.* **1995**, *52*, 178–188.
- (49) Mills, G.; Schenter, G. K.; Makarov, D. E.; Jónsson, H. Generalized Path Integral Based Quantum Transition State Theory. *Chem. Phys. Lett.* **1997**, *278*, 91–96.
- (50) Zhang, Y.; Stecher, T.; Cvitaš, M. T.; Althorpe, S. C. Which Is Better at Predicting Quantum-Tunneling Rates: Quantum Transition-State Theory or Free-Energy Instanton Theory? *J. Phys. Chem. Lett.* **2014**, *5*, 3976–3980.
- (51) Markland, T. E.; Habershon, S.; Manolopoulos, D. E. Quantum Diffusion of Hydrogen and Muonium Atoms in Liquid Water and Hexagonal Ice. *J. Chem. Phys.* **2008**, *128*, 194506–194516.
- (52) Shelton, G. R.; Hrovat, D. A.; Borden, W. T. Tunneling in the 1,5-Hydrogen Shift Reactions of 1,3-Cyclopentadiene and 5-Methyl-1,3-Cyclopentadiene. *J. Am. Chem. Soc.* **2007**, *129*, 164–168.
- (53) Shelton, G. R.; Hrovat, D. A.; Borden, W. T. Calculations of the Effect of Tunneling on the Swain-Schaad Exponents (SSEs) for the 1,5-hydrogen Shift in 5-methyl-1,3-cyclopentadiene. Can SSEs Be Used to Diagnose the Occurrence of Tunneling? *J. Am. Chem. Soc.* 2007, 129, 16115–16118.
- (54) Markland, T. E.; Manolopoulos, D. E. An Efficient Ring Polymer Contraction Scheme for Imaginary Time Path Integral Simulations. *J. Chem. Phys.* **2008**, *129*, 024105–024114.
- (55) Marsalek, O.; Markland, T. E. Ab initio molecular dynamics with nuclear quantum effects at classical cost: Ring polymer contraction for density functional theory. *J. Chem. Phys.* **2016**, *144*, 054112–054122.
- (56) CPMD, IBM Corp 1990–2008, MPI Für Festkörperforschung Stuttgart 1997–20011.
- (57) Martyna, G. J.; Tuckerman, M. E. A Reciprocal Space Based Method for Treating Long Range Interactions in Ab Initio and Force-field-based Calculations in Clusters. *J. Chem. Phys.* **1999**, *110*, 2810–2821.
- (58) Troullier, N.; Martins, J. L. Efficient Pseudopotentials for Plane-wave Calculations. *Phys. Rev. B: Condens. Matter Mater. Phys.* **1991**, 43, 1993–2006.

- (59) Berne, B. J.; Thirumalai, D. On the Simulation of Quantum Systems: Path Integral Methods. *Annu. Rev. Phys. Chem.* **1986**, 37, 401–424.
- (60) Martyna, G. J.; Klein, M. L.; Tuckerman, M. E. Nosé-Hoover Chains: The Canonical Ensemble via Continuous Dynamics. *J. Chem. Phys.* **1992**, *97*, 2635–2643.
- (61) Tuckerman, M. E.; Marx, D.; Klein, M. L.; Parrinello, M. Efficient and General Algorithms for Path Integral Car-Parrinello Molecular Dynamics. *J. Chem. Phys.* **1996**, *104*, 5579–5588.
- (62) Frisch, M. J.; Trucks, G. W.; Schlegel, H. B.; Scuseria, G. E.; Robb, M. A.; Cheeseman, J. R.; Scalmani, G.; Barone, V.; Mennucci, B.; Petersson, G. A. et al. *Gaussian 09*, Revision E.01.; Gaussian Inc. Wallingford, CT, 2009.
- (63) Ryckaert, J.-P.; Ciccotti, G.; Berendsen, H. J. Numerical Integration of the Cartesian Equations of Motion of a System with Constraints: Molecular Dynamics of N-alkanes. *J. Comput. Phys.* **1977**, 23, 327–341.
- (64) Tuckerman, M. E.; Parrinello, M. Integrating the Carparrinello Equations. Ii. Multiple Time Scale Techniques. *J. Chem. Phys.* **1994**, *101*, 1316–1329.